Science Advances
AAAS

Supplementary Materials for

Melt electrowriting enabled 3D liquid crystal elastomer structures for cross-scale actuators and temperature field sensors

Xueming Feng *et al.*

Corresponding author: Li Wang, wanglime@mail.xjtu.edu.cn

Sci. Adv. **10**, eadk3854 (2024)
DOI: 10.1126/sciadv.adk3854

The PDF file includes:

Other Supplementary Material for this manuscript includes the following:

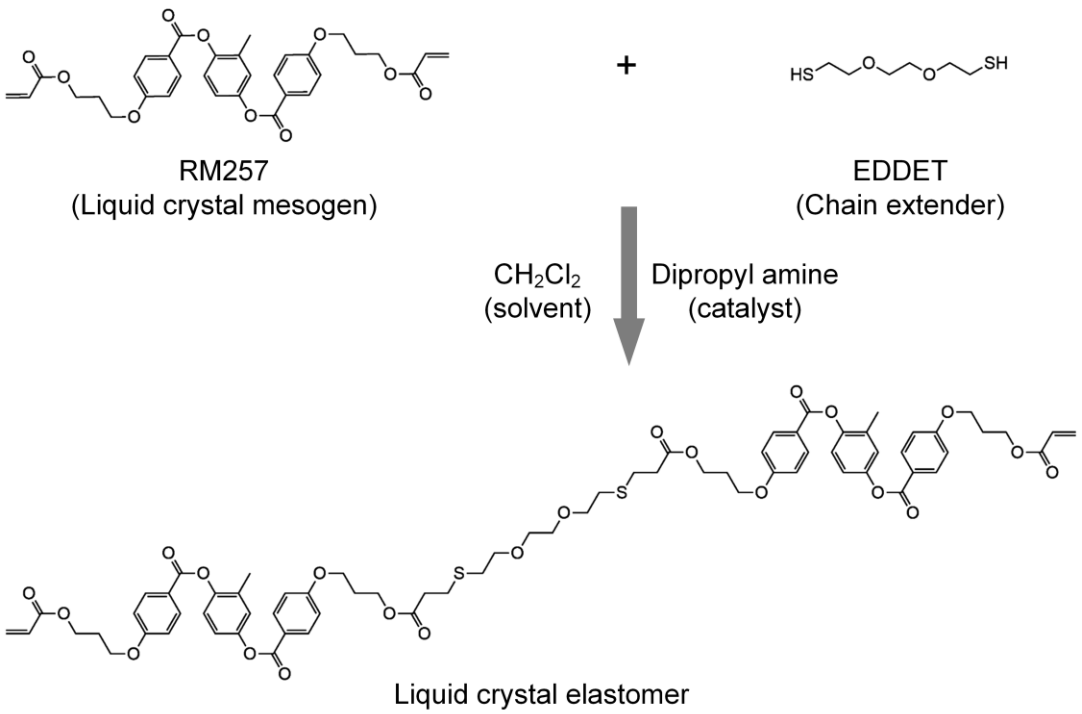

Fig. S1. Chemical component of LCE ink. The preparation of LCE ink by the Michael addition reaction between liquid crystal mesogens RM257 and chain extender EDDET. CH_2Cl_2 is used as solvent, and dipropyl amine is the catalyst.

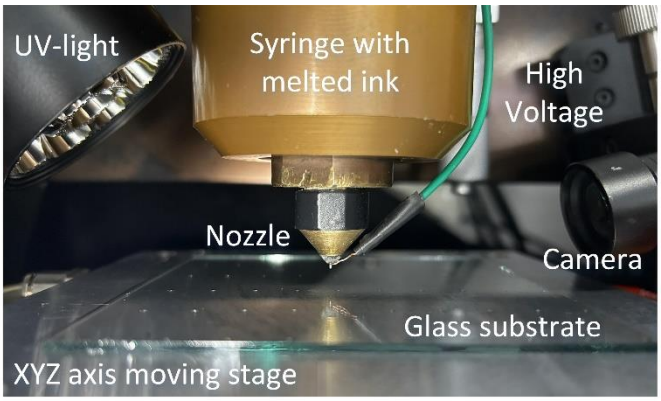

Fig. S2. Components of the MEW 3D printing equipment. The components include: (1) a heating chamber, which is used to heat the LCE ink to a specified temperature; (2) a syringe which is connected with a metal nozzle, is used to hold the melted LCE ink; (3) an air for controlling the flow rate of the LCE ink through the adjustment of the air pressure inside the heating chamber; (4) a high-voltage power supply to provide the necessary electrical potential for generating the electric field between the metal nozzle and the substrate; (5) a glass substrate, placed on the moving stage, serves as a platform for the deposition and solidification of LCE ink to form desired structures; (6) a UV lamp for curing the LCE ink; (7) a three-axis moving stage to govern the printing path, speed, and other parameters, which are typically controlled through G-code instruction; and (8) a high precision industrial camera for observing the LCE microfibers.

Fig. S3. Stable LCE micro-jet during the MEW printing process. The LCE micro-jet was jetted from a nozzle with an inner diameter of approximately 200μm and underwent continuous reduction in diameter. By the time it deposits onto the substrate, its diameter decreased to only 20μm.

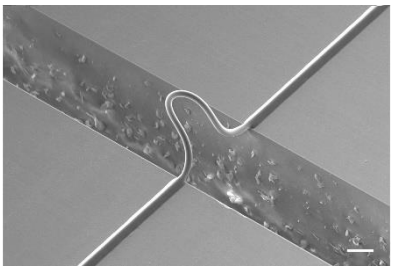

Fig. S4. MEW printed single LCE microfiber with a diameter of around 30µm. The microfiber was printed using a 26G nozzle, with a printing temperature set at 80°C. The printing speed was controlled at 3mm/s, while the air pressure was maintained at 0.2MPa. The nozzle was connected to a constant high-voltage of 2.5 kV.

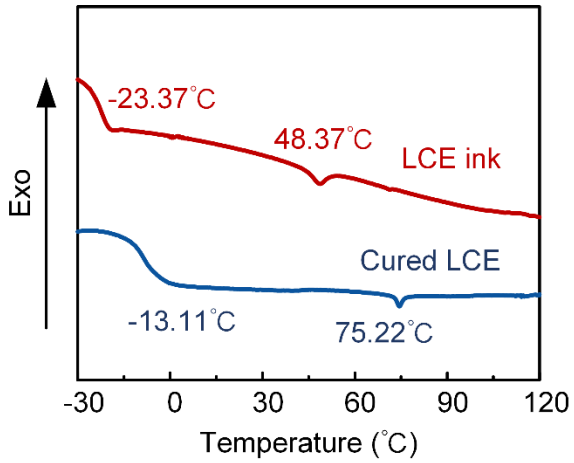

Fig. S5. Differential scanning calorimeter (DSC) test of the LCE ink and cured LCE structures. The glass transition temperature (T_g) and the nematic-isotropic phase transition temperature (T_{NI}) of the LCE ink are -23.37℃ and 48.37℃, respectively. After the LCE ink is printed and cured using UV-light, the T_g and T_{NI} values increase to -13.11℃ and 75.22℃, respectively.

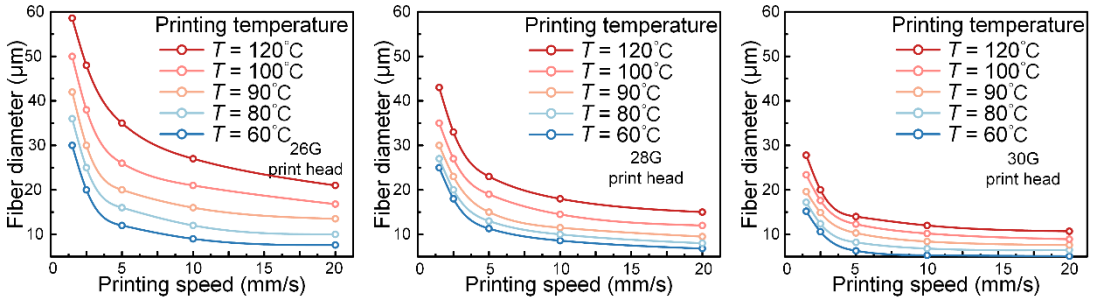

Fig. S6. The impact of nozzle diameter, printing speed and printing temperature on the microfiber diameter. The diameter of the LCE microfiber printed using a 28G nozzle exhibits a decrease when the printing speed is increased or the printing temperature is decreased. We achieved a minimum diameter of 4.5μm for the MEW printed microfiber. This was obtained using a 30G nozzle, with a printing speed of 20mm/s and a printing temperature of 60℃. On the other hand, the maximum diameter of the fabricated microfiber was 60μm, which was obtained using a 26G nozzle, with a printing speed of 1mm/s and a printing temperature of 120℃.

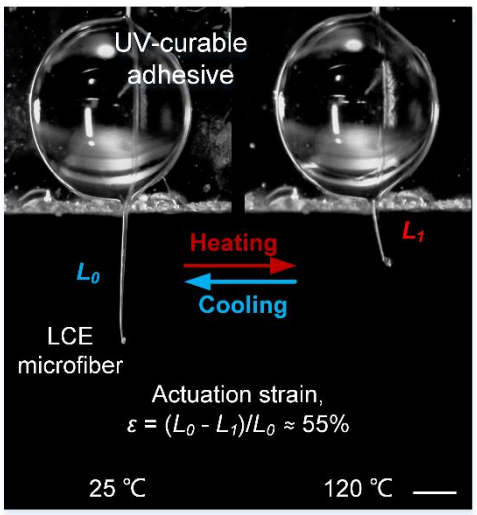

Fig. S7. Actuation strain measurement of a single LCE microfiber. In our experiment, the maximum strain value of the LCE microfiber was 55%. The LCE microfiber was printed at a printing speed of 20mm/s and a printing temperature of 90℃.

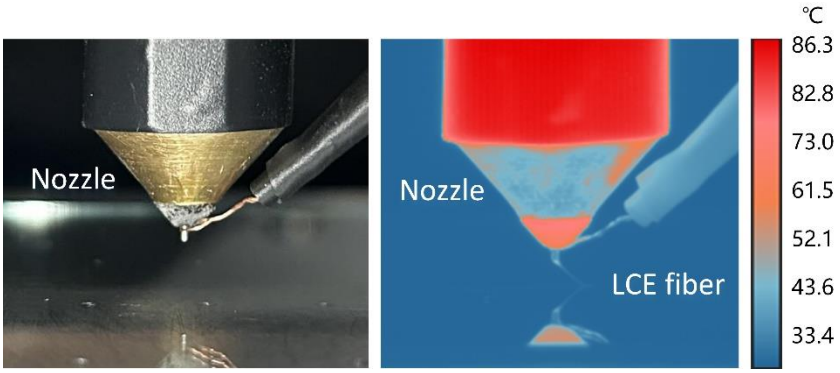

Fig. S8. The temperature distribution of the nozzle and the LCE micro-jet. During the MEW 3D printing process, the temperature distribution of the nozzle and the LCE micro-jet can be visualized in the temperature mapping diagram. When the heating chamber was set to 90°C, the temperature at the nozzle was approximately 50°C, while the ejected LCE micro-jet decreased to around 40°C.

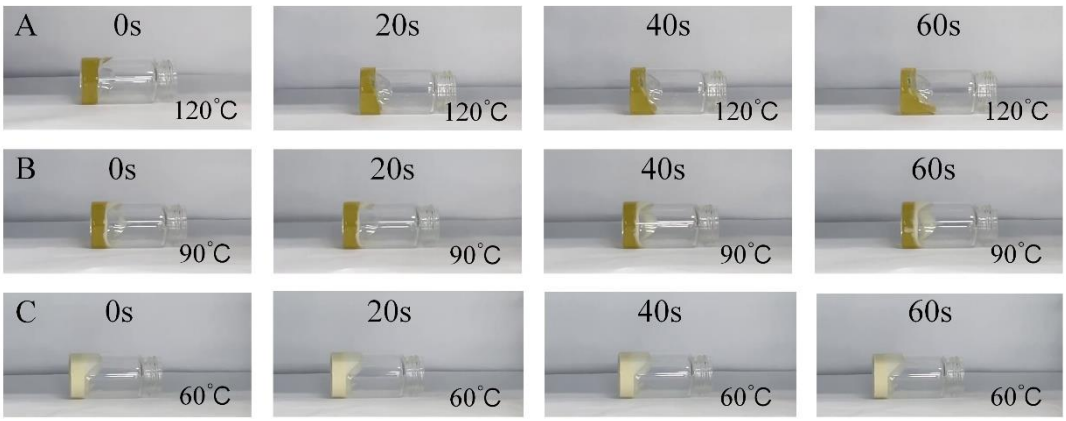

Fig. S9. The flowability test of LCE printing ink. At low temperatures, LCE ink tends to exhibit a cloudy appearance. In contrast, at elevated temperatures, mesogens within LCE experience increased freedom of movement, allowing light to pass through more smoothly. As a consequence, the material appears transparent. We heated LCE ink separately to 120°C, 90°C, and 60°C. Following this, we deactivated the heater, positioned it horizontally, and evaluated the flow behavior of the LCE ink under the influence of gravity, simulating the process of LCE ink being extruded from the heating chamber, entering the print nozzle, and being expelled from the nozzle. Clearly, when the LCE material was heated to 120°C, the ink was in a transparent state and rapidly flows horizontally within 60 seconds. At 90°C, the material still maintained transparency, but its flowability was significantly reduced. When the ink was heated to 60°C, the material was in an opaque and turbid state with almost no flowability. At this temperature, LCE mesogens were completely fixed in position.

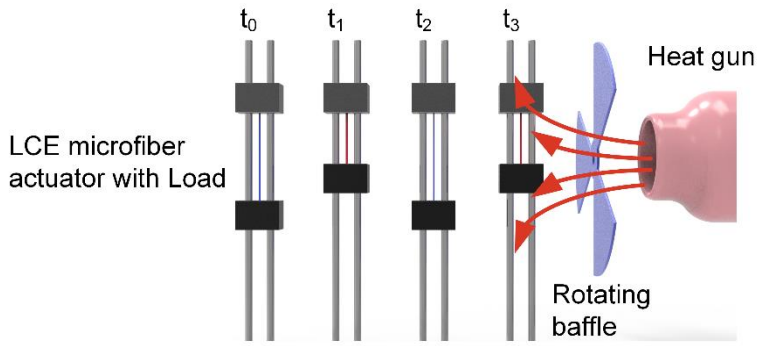

Fig. S10. Illustration of the rapid response capability testing of the LCE microfiber actuator. We placed a slider between two metal rails and suspended the LCE microfiber to lift the slider, allowing it to move rapidly up and down under thermal airflow stimuli. We employed a heat gun as the heat source for thermal airflow stimuli and used a rotating baffle to control the frequency of the airflow. The LCE microfiber actuator was subjected to thermal airflow, causing it to lift and lower a weight in response.

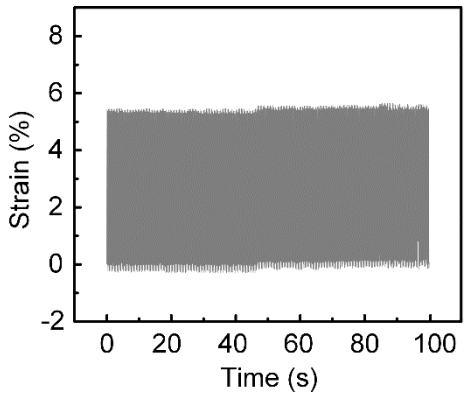

Fig. S11. Long-term durability testing of LCE microfibers actuated under cyclic external loads. The frequency of thermal airflow is 10Hz. The weight of the slider (weight 150 mg, applied stress 0.4 MPa) is over 3500 times greater than the weight of the fiber actuator (length 10 mm, diameter 22 μm, weight 0.042 mg). The microfiber maintained its actuation strain without significant signs of fatigue even after 10,000 cycles.

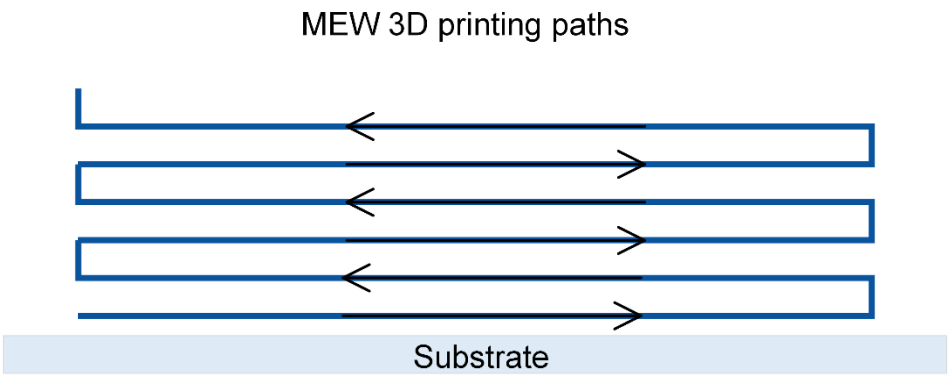

Fig. S12. MEW 3D printing path. By continuously stacking microfibers back and forth at the same location, we can create wall-like structures with a high aspect ratio, where the height can be precisely controlled.

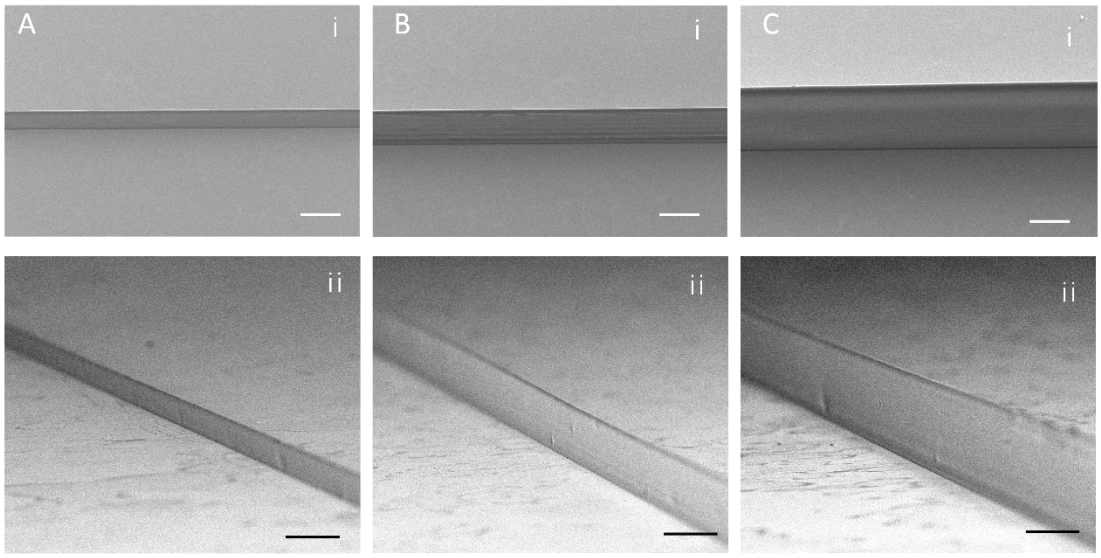

Fig. S13. The SEM images of several LCE wall structures. We printed three wall structures with different layers using the same printing parameters. All figures labeled as i are front views, while all figures labeled as ii are side views. As depicted in the figures, the MEW-printed LCE wall structures exhibited uniformity and structural integrity over a large scale, without any defects. Scale bar, 300 μm.

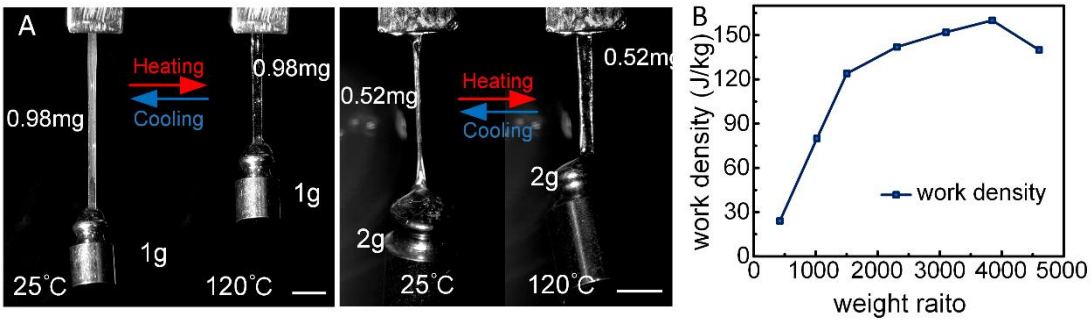

Fig. S14. Testing process and results of LCE actuators lifting loads. (A) Optical images of the LCE actuators under different loads. The left image shows a LCE strip actuator (0.98 mg) lifting a 1g load, with a strain of around 40% and work density of around 80 J kg^{-1}. The right image shows a LCE strip actuator (0.52 mg) lifting a 2 g load, exceeding its own weight by 3800 times, with a strain of around 24% and work density reaching its highest value of 160 J kg^{-1}. The lifting process can be seen in Supplementary video 5. Scale bar, 5 mm. (B) The work density of MEW-printed LCE actuators under various loads.

Table S1. The actuation strain, work density, and corresponding resolution were compared between the previously reported LCE actuators and the MEW printed LCE actuators in this study.

Reference	Actuation strain (%)	Work density (J/kg)	Resolution (μm)
Voxelated liquid crystal elastomer film (*13*)	55	2.6	50
DLP printed LCE artificial muscle (*24*)	50	63	10
Human muscle (*37*)	20	40	---
Layered LCE actuators (*38*)	50	20	50
DIW 3D printed LCE actuators with spatially programed nematic order (*39*)	43.6	39	100
2-photon direct laser writing microstructured LCE film *(40)*	40	20	2.9
LCE/CNT composite filament actuators (*41*)	53	55	~400
DIW 3D printed LCE actuators with closed loop control (*42*)	51	40.7	930
LCE-Liquid metal composited actuators (*43*)	13.5	2	45
LCE- triethylene glycol (TUEG) artificial muscle (*44*)	35	65	400
This work	50	160	4.5

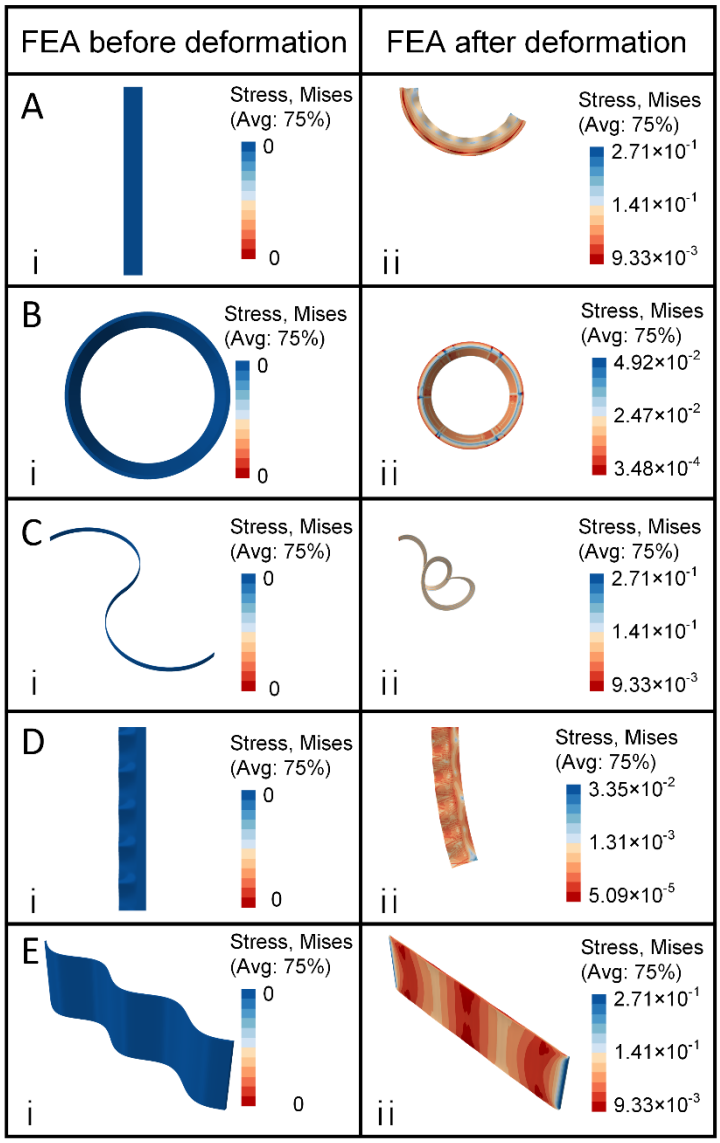

Fig. S15. The comparative FEA images of the deformation of the elementary structural units before and after heating. The FEA images of several LCE elementary structural units with graded size and actuation strain, including (A) the LCE strip with a varying actuation strain, (B) the LCE cylindrical structure, (C) the LCE spring-shaped structure, (D) the sinusoidal LCE structure, and (E) the size-graded sinusoidal LCE curved strip.

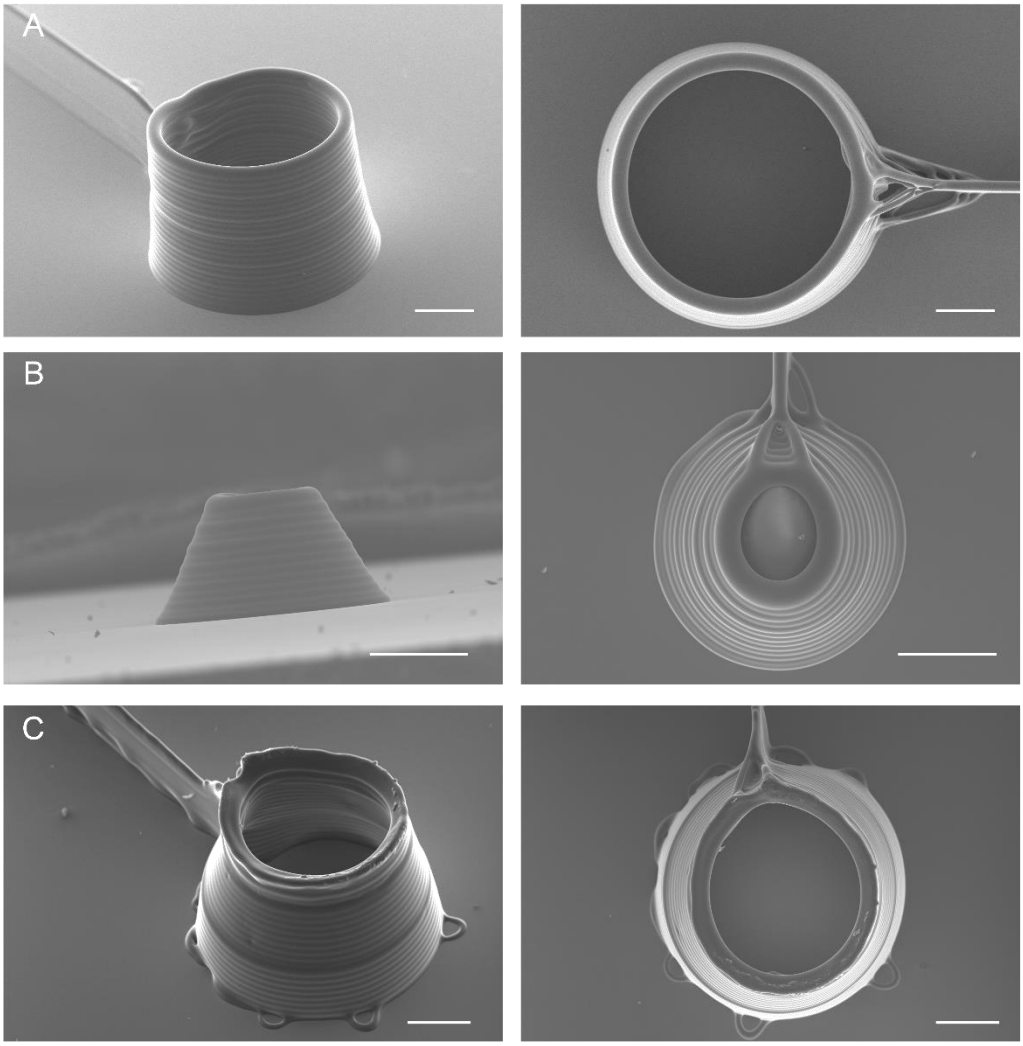

Fig. S16. The SEM images of several cylinder structures with varying diameters. (A) The SEM images of cylinder structure with a small diameter. (B) The SEM images of a pyramid-shaped cylindrical structure with gradually decreasing diameters. (C) The SEM images of a gourd-shaped cylindrical structure with diameters first decreasing and then increasing. Scale bar, 500 μm.

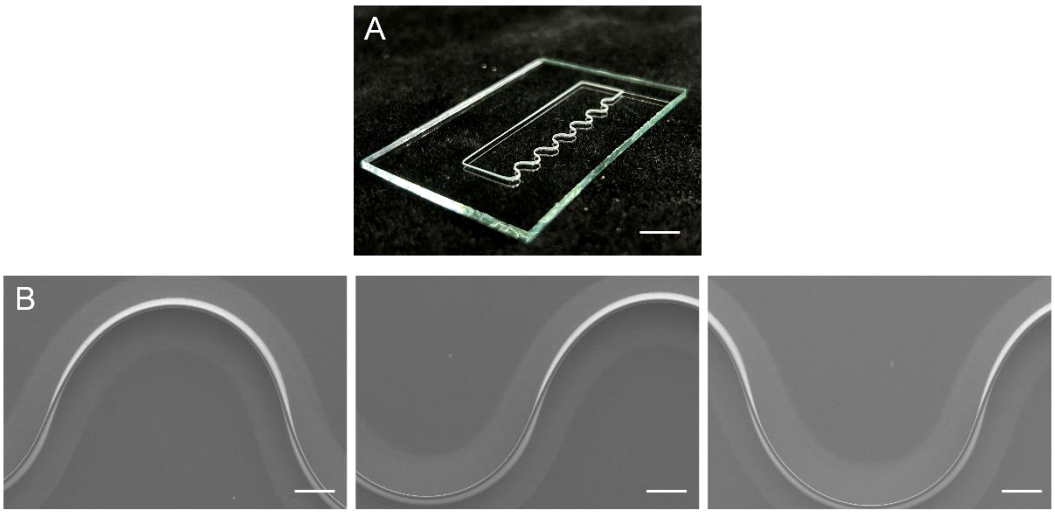

Fig. S17. The photograph and SEM images of the S-shaped structure. (A) The photograph of the S-shaped structure with varying actuation strains on its top (50%) and bottom sides (30%). Scale bar, 2mm. (B) The SEM images of the S-shaped structure. Scale bar, 500 μm.

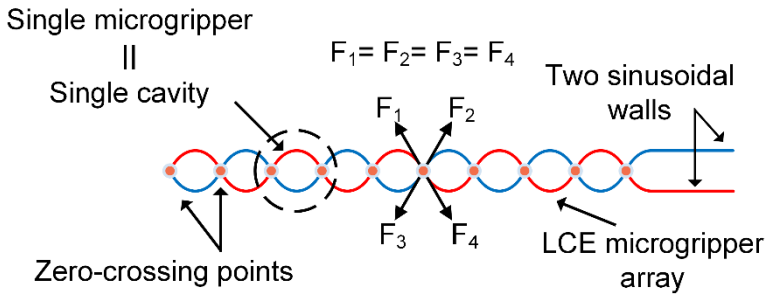

Fig. S18. The MEW 3D printing paths for the fabrication of LCE microgripper array. we combined and fabricated two LCE sinusoidal walls via layer-by-layer printing on a substrate, resembling the leaves of the flytrap. During the MEW 3D printing, the zero-crossing positions of the two sinusoidal walls were ensured to intersect and adhere together. In this way, an array of microgrippers was formed, with each small cavity representing an individual LCE microgripper.

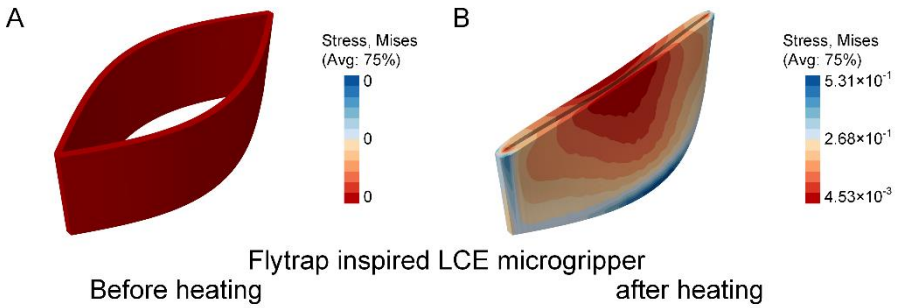

Fig. S19. FEA of the contraction of the flytrap-inspired LCE microgripper before and after heating. After heating, the bottom of the LCE microgripper firmly adheres to the substrate without contraction. Meanwhile, the top of the microgripper experiences thermal contraction and gradually straightens due to balanced forces at the zero-crossing points of the LCE sinusoidal walls.

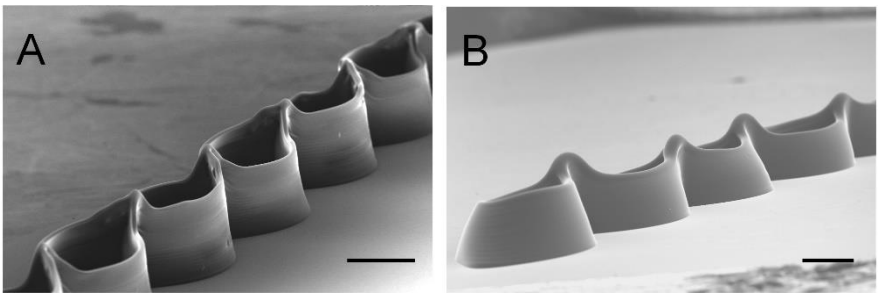

Fig. S20. SEM images of the microgripper arrays. (A) Microgrippers with a size of 3 mm in length, 2 mm in width, and 2 mm in height. Scale bar, 1 mm. (B) Microgrippers with of 1.5 mm in length, 1 mm in width, and 1 mm in height. Scale bar, 500 μm.

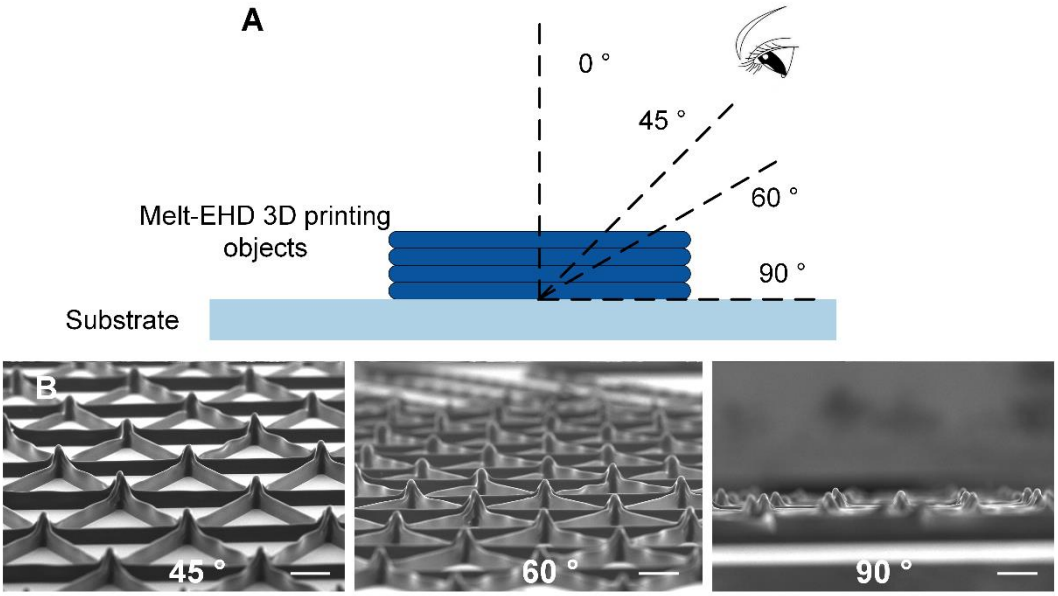

Fig. S21. The SEM images of a triangular LCE lattice structure observed from different viewing angles. (A) Schematic diagram illustrating the observation of an object using SEM from different viewing angles. (B) SEM images of the triangular LCE lattice structure observed from different viewing angles (45 °, 60 °, 90 °). The 3D lattice structure fabricated through MEW 3D printing exhibited a remarkable consistency in height over a large area.

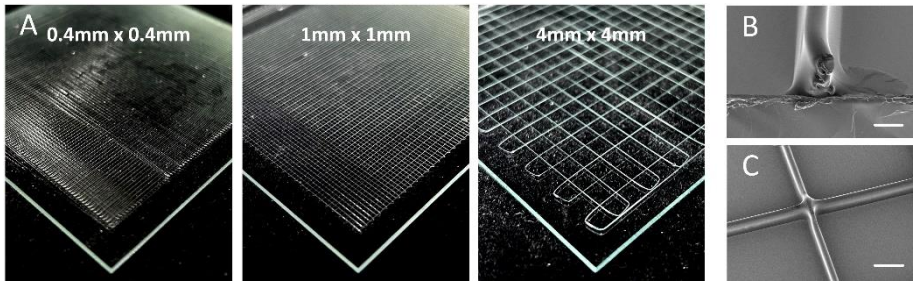

Fig. S22. The optical images and SEM images of LCE grids. (A) The optical images of LCE grids with different grid spacings are shown. The grid spacings can be adjusted freely using MEW 3D printing process. In this work, we presented LCE grids with the minimum spacing of 0.4 mm × 0.4 mm, the spacing of 1 mm × 1mm, and the maximum spacing of 4 mm × 4 mm. (B) The cross-sectional SEM image of an individual LCE wall structure forming the grids is shown. It can be observed that each LCE wall structure is composed of three layers of LCE microfibers (with a diameter of around 30 μm). Scale bar, 50 μm. (C) The SEM image displays the intersection of two perpendicular LCE wall structures within the LCE grid. The two LCE wall structures were firmly connected together at the crossing point. Scale bar, 100 μm.

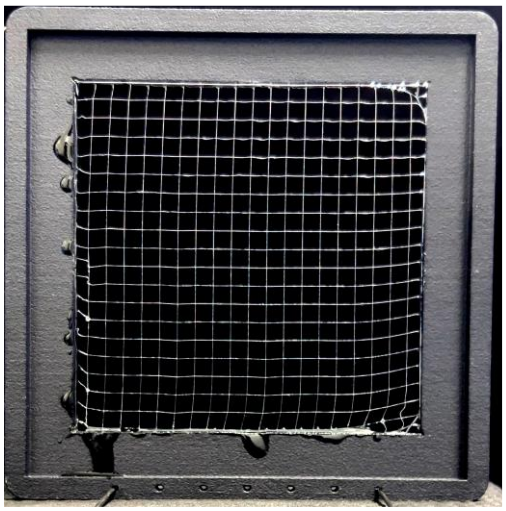

Fig. S23. Photograph of the LCE grid transferred and adhered to a nylon frame. The LCE grid is first 3D printed and cured on a glass substrate, then peeled off and transferred onto a hollow nylon frame. The grid is securely affixed around its edges using UV adhesive. As a result, the suspended LCE grid in the middle of the frame can undergo thermal deformation.

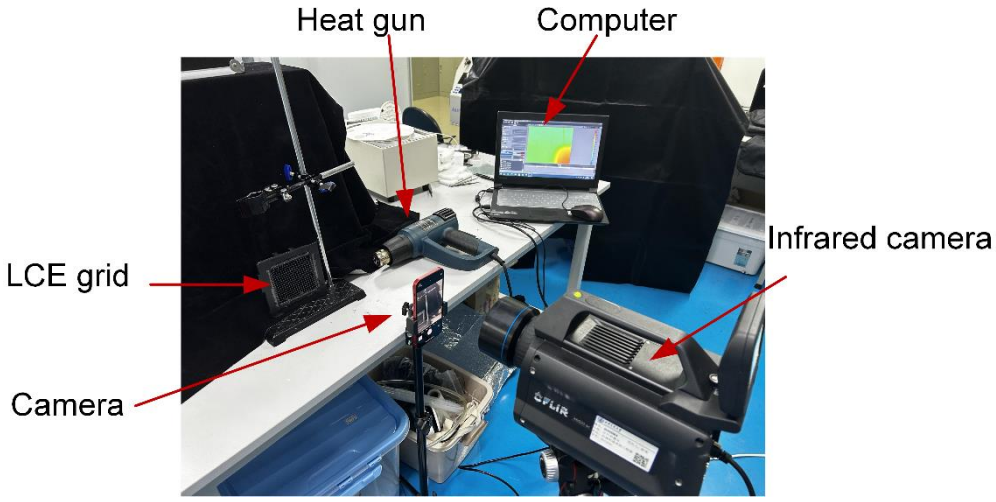

Fig. S24. Devices of dataset construction process of temperature field sensors. In this study, we simulated changes in the temperature field by using a heat gun with a temperature range of 100 to 550°C to blow hot air at different temperatures. The deformation of the LCE grid was captured using an iPhone 14 camera. Real-time temperature measurements of the grid were obtained using an infrared camera (X6520sc). The infrared camera was controlled by a computer.

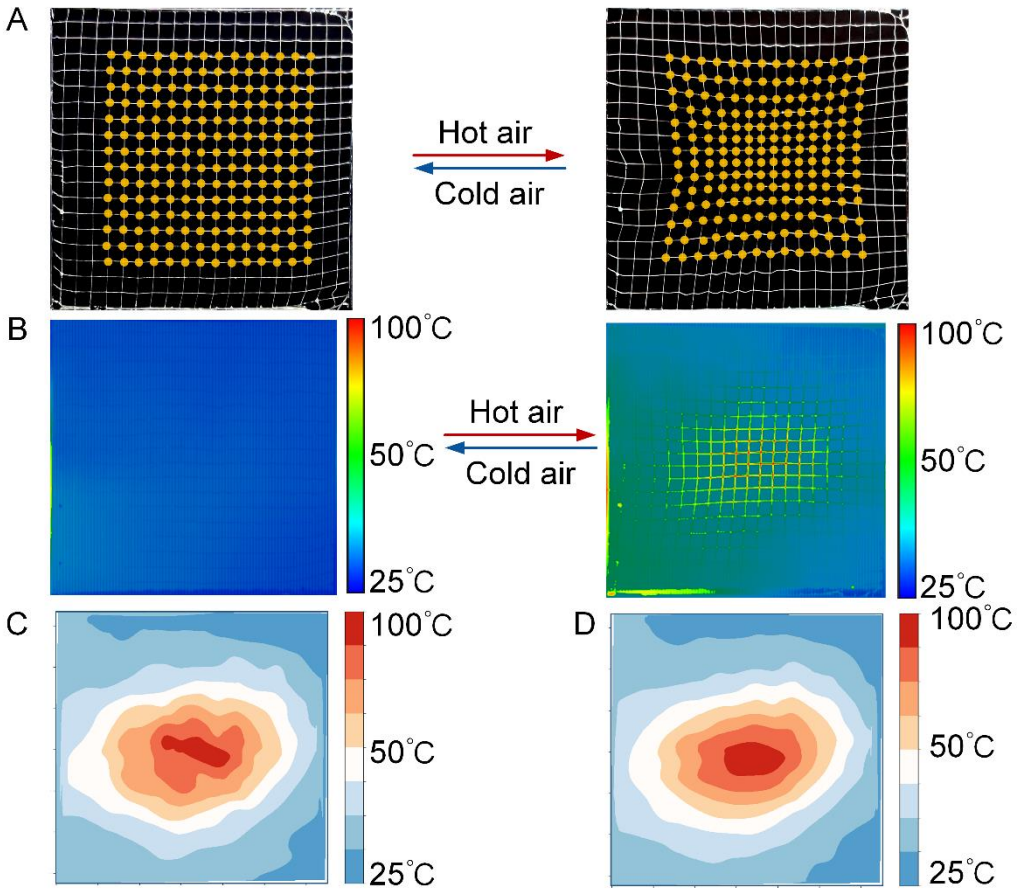

Fig. S25. The construction process of the dataset for the DL model. In this experiment, the LCE grid is exposed to a heat gun blowing hot airflow directly at its center, the temperature at the airflow center is around 100°C. (A) The photographs of the LCE grid before and after deformation were captured using a camera. (B) The infrared images were captured using the infrared camera before and after the deformation of the LCE grid. (C) The contour plot of the measured temperature field is generated based on the measured temperature field of all the nodes. (D) Based on the deformation images of the LCE grid, the deep learning model was utilized to analyze and generate the predicted ambient temperature contour map.

In this study, we used the camera of an iPhone 14 to capture RGB images with a resolution of 2160x3840 and an infrared thermal imaging camera to capture infrared temperature images with a resolution of 600x500. Prior to further analysis, we conducted pre-processing on the images. First, we utilized the four corners of the metal frame as registration markers and performed perspective transformation to convert the region of the grid material in the RGB image to a 1000x1000 resolution picture. Subsequently, we applied median filtering and contrast enhancement to enhance the quality of the images. To reduce computational complexity, we employed grayscale gradient detection to detect lines in the images and merged adjacent lines. Next, we calculated the intersection node between the lines and merged duplicate nodes, completing the automatic extraction of the nodes in the grid material.

In order to minimize the impact of the nylon frame on the edge grids, we selected the 14x14 grid intersections in the center as the temperature sampling points. Using perspective transformation, we transformed the grid intersections from the RGB image coordinate system to the infrared image coordinate system to read the corresponding temperatures. For each frame of the image, we collected the RGB image coordinates (x, y) and the corresponding temperature (t) of the 14x14 grid intersections to create a dataset with a total of 1355 frames. To reduce the uncertainty caused by random sampling, we used stratified random sampling and divided the dataset into training and testing datasets in an 8:2 ratio.

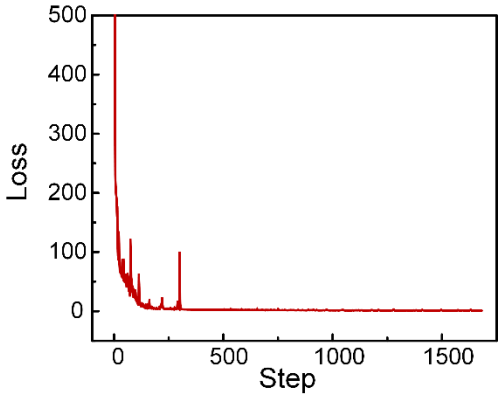

Fig. S26. Loss function curve in the training process of DL model. The Loss values steadily decrease as the number of training steps increases. Despite occasional fluctuations in the intermediate stages, the overall trend shows a clear decrease, indicating that the model is effectively converging during training. Eventually, the loss value stabilizes at approximately 0.89, indicating that the model has converted to a satisfactory level.

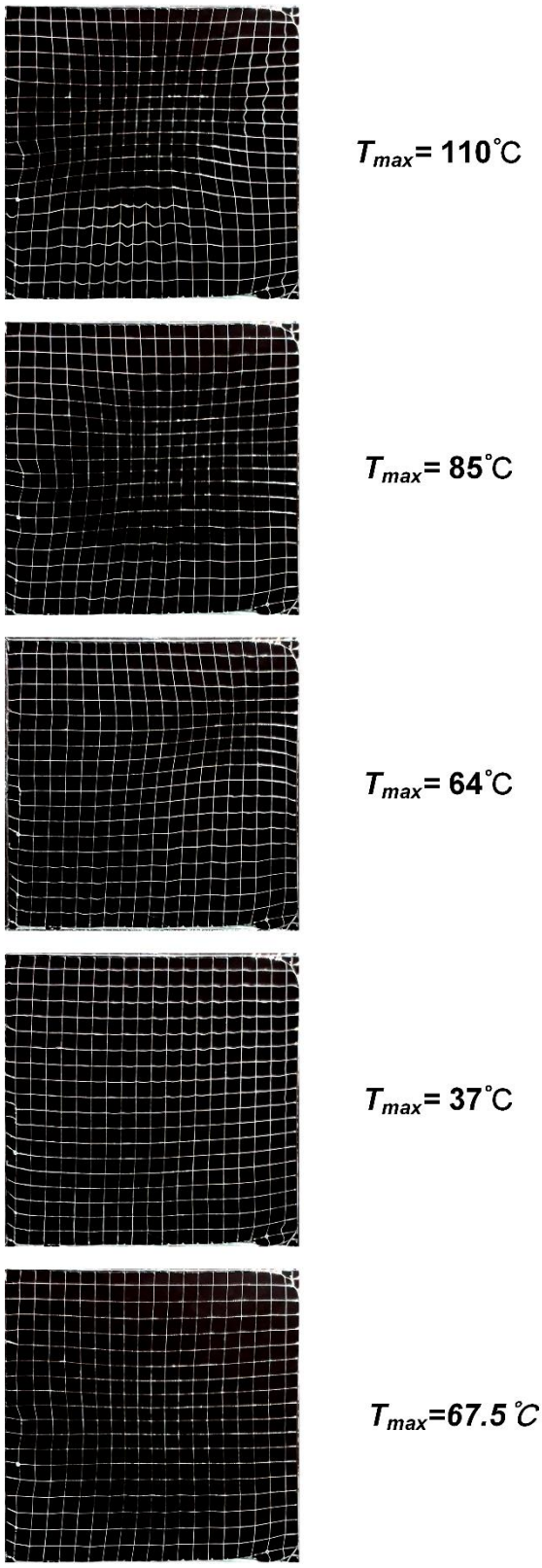

Fig. S27. The LCE grid deformation images captured by camera. The five inferred temperature maps in Fig. 5E are generated through the pre-trained DL model based on these five LCE grid deformation images.

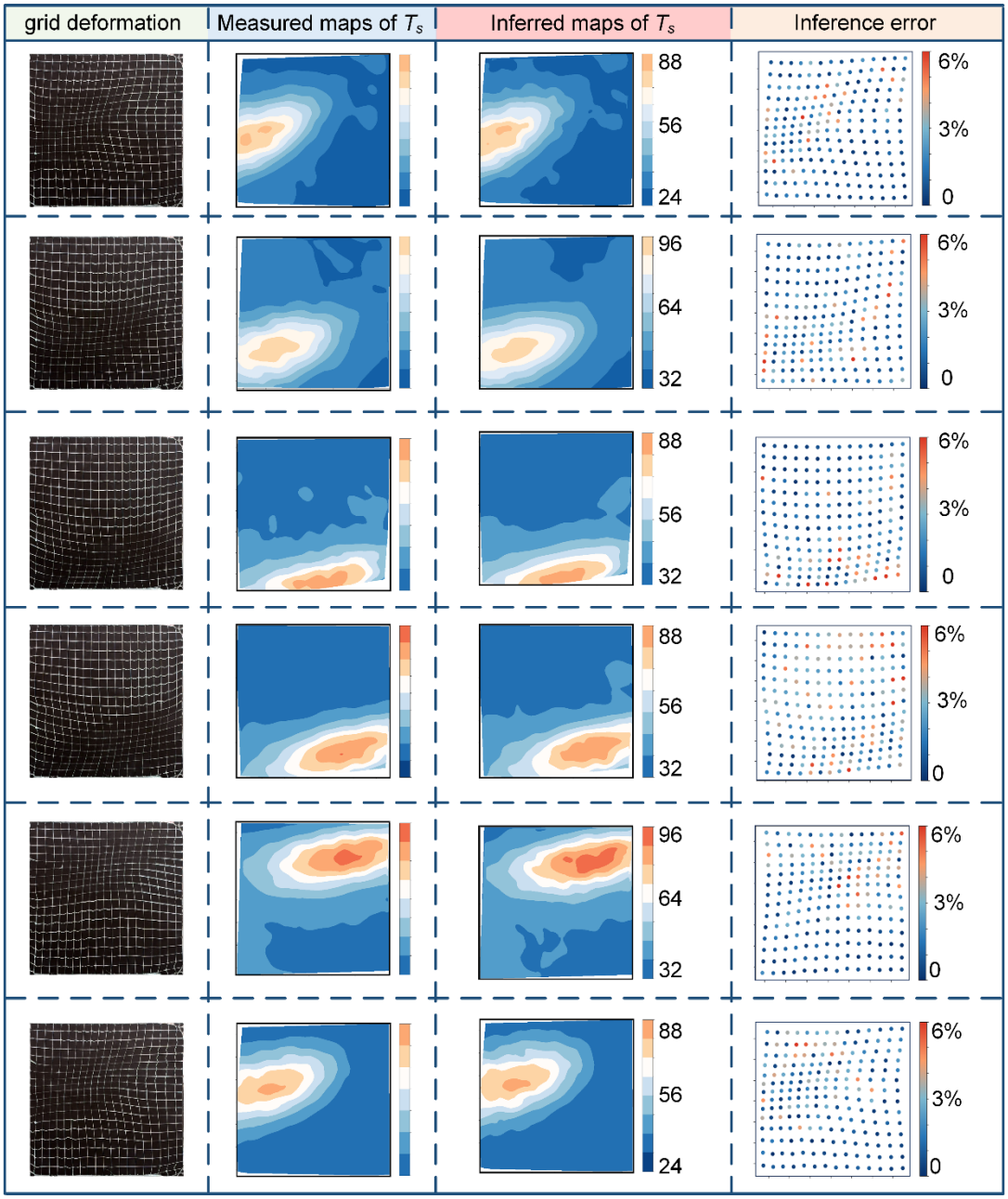

Fig. S28. The performance of the STF sensor with variations in the placement of the high-temperature zone at the periphery of the LCE grid for the hot airflow. As evident from the accompanying figures, for a temperature field distribution characterized by a significant temperature difference (T_{max} is around 90 °C, with a temperature difference of around 60°C) and a relatively compact high-temperature region, the Inferred maps and Measured maps exhibit a high degree of consistency, with inferred temperature errors consistently below 6%. This underscores the STF sensor's capability to achieve high-precision sensing of complex temperature fields across extensive areas.

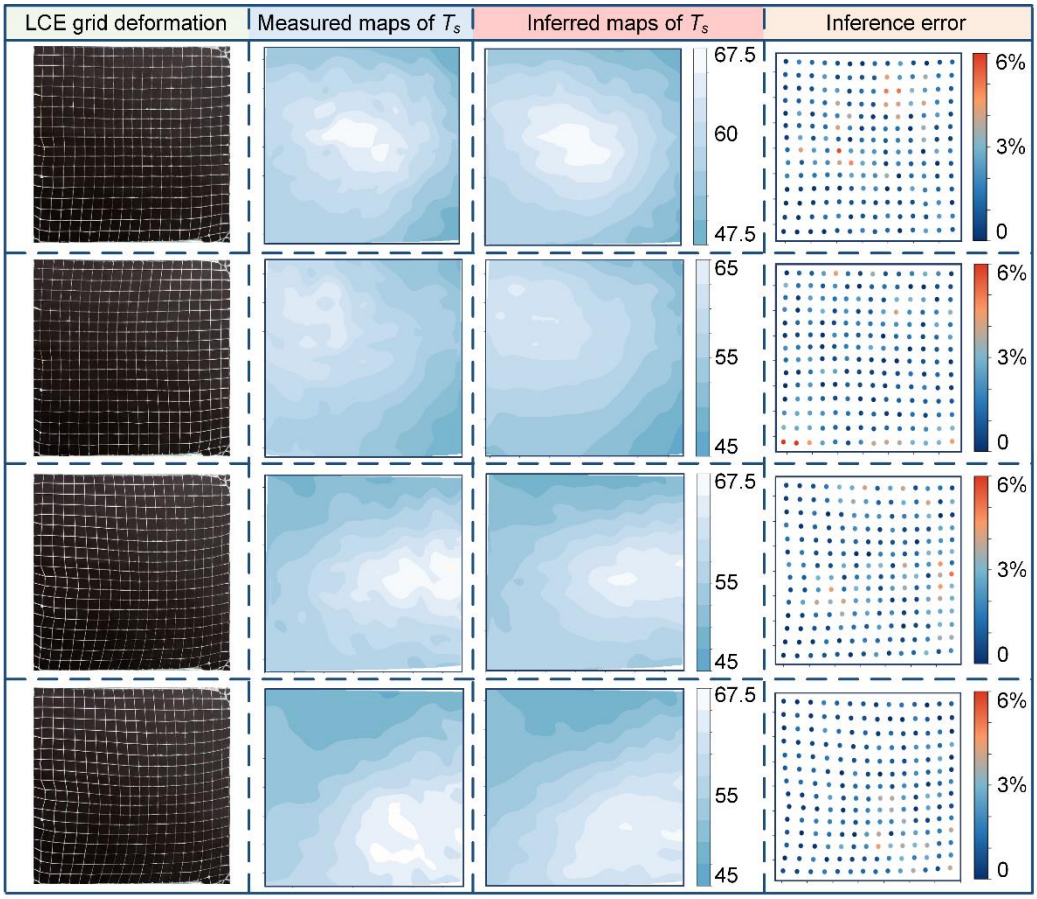

Fig. S29. The performance of the STF sensor with different high-temperature zone placements is shown when the entire LCE grid is exposed to the hot airflow. As a result, the average temperature of the LCE grid reaches 55℃, and the temperature difference across the entire grid is approximately 20℃. Despite this, the STF sensor maintains high-precision detection of the large-area uniform temperature field, and the inference error of all nodes does not exceed 6%.

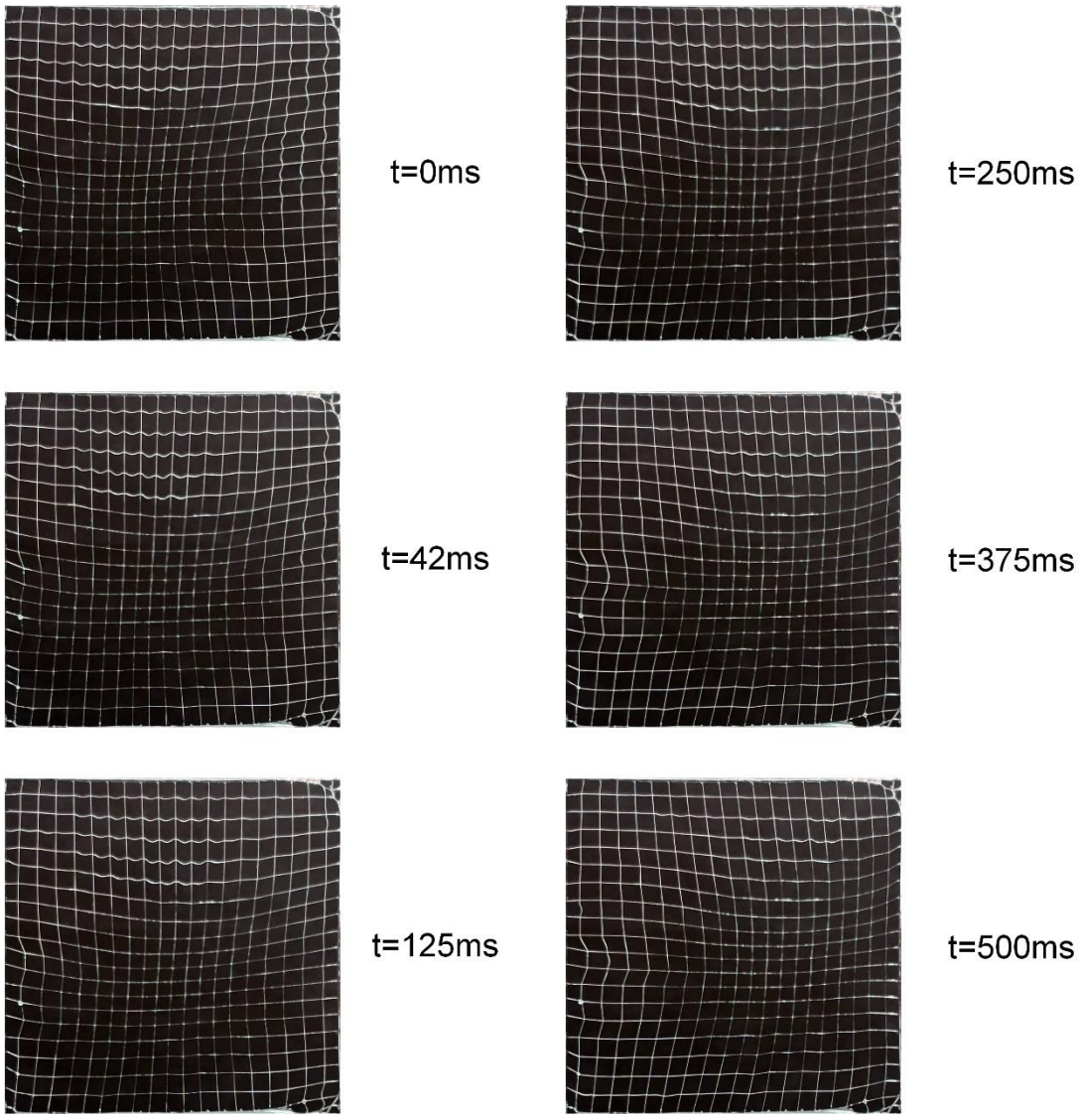

Fig. S30. The LCE grid deformation images during high-temperature field rapid response test. The deformation images of the temperature fields with high-temperature zones (T_{max} of 100°C with a significant temperature difference of 60°C), traversing from left to right across the STF sensor.

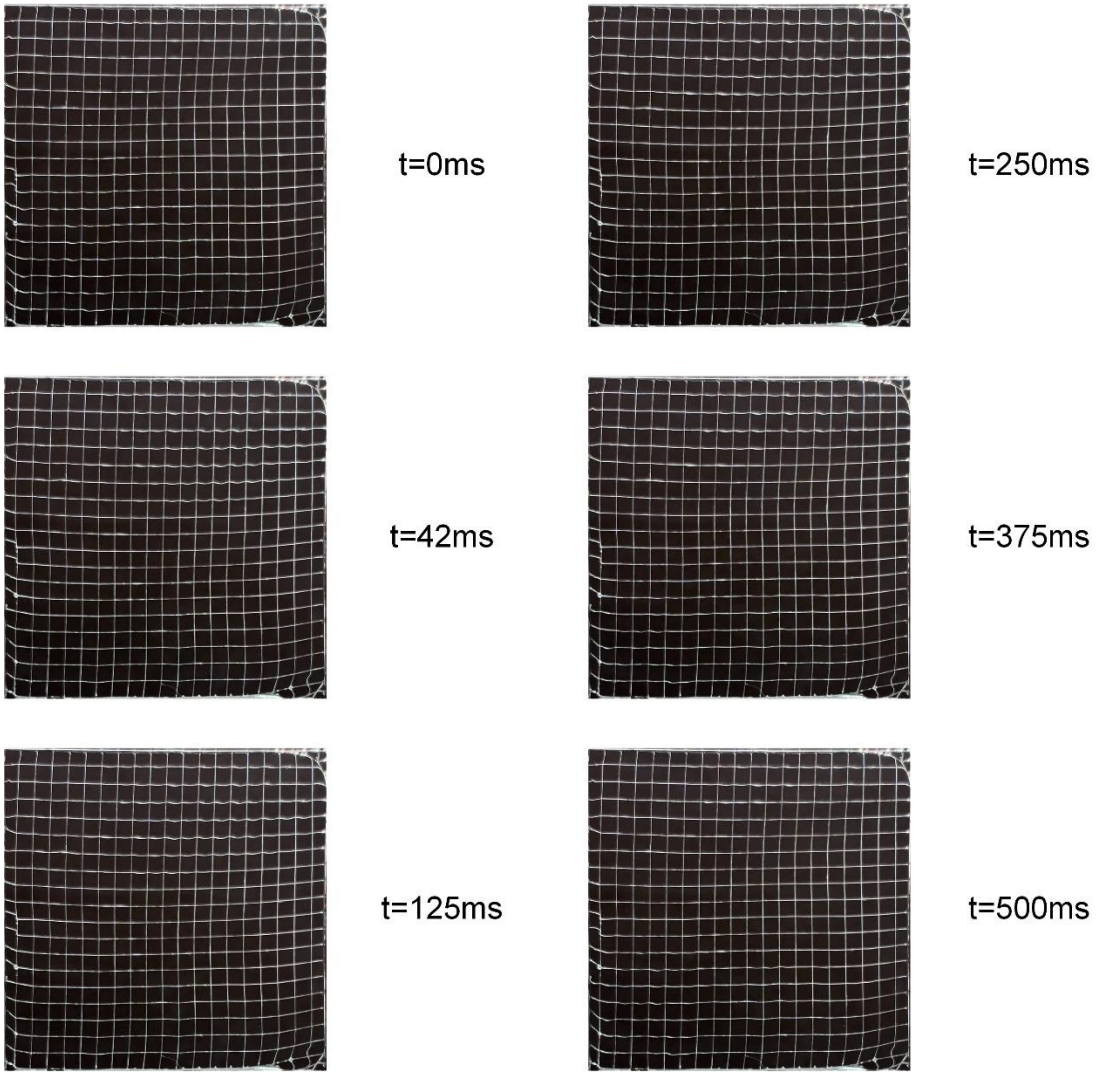

Fig. S31. The LCE grid deformation images during low-temperature field rapid response test. The deformation images of the temperature fields with high-temperature zones (T_{max} of 36°C with a low-temperature difference of 6°C), traversing from bottom to top across the STF sensor.

Video S1. Melt electrowriting 3D printing process
Video S2. Actuation strain test of a single LCE microfiber
Video S3. Strain test of LCE fiber actuators under different loads
Video S4. Actuation performance of LCE microfiber under thermal airflow stimuli with different frequencies
Video S5. Strain measurement of LCE wall structure and Actuation strains of LCE wall structures with different loads
Video S6. Deformation of various elementary structural units
Video S7. Reversibly Opening and closing processes of the LCE microgripper
Video S8. LCE microgripper reversibly catches and releases an object
Video S9. Deformation of various 3D LCE lattice structures
Video S10. The construction process of the dataset for the DL model of the STF sensor